

8. G. Efstathiou, in *Les Houches, Session LX: Cosmology and Large Scale Structure*, R. Schaeffer et al., Eds. (North-Holland, Amsterdam, 1996), pp. 107–252.

9. K. B. Fisher, M. Davis, M. Strauss, A. Yahil, J. Huchra, *Mon. Not. R. Astron. Soc.* **267**, 927 (1994).

10. V. K. Narayanan, A. Berlind, D. H. Weinberg, available at <http://xxx.lanl.gov/abs/astro-ph/9812002>.

11. G. Kauffmann, J. M. Colberg, A. Diaferio, S. D. M. White, *Mon. Not. R. Astron. Soc.* **303**, 188 (1999). To linear bias enthusiasts, this result may appear puzzling. A textbook example of such a possibility is the spatial distribution of the gas and stars in a galaxy. Their distribution itself is biased, whereas their relative velocities at separations comparable to the radius of the dark halo are not.

12. M. A. Strauss and J. A. Willick, *Phys. Rep.* **261**, 271 (1995).

13. N -body simulations show that the stable clustering solution [$u_{12} = 0$, $-v_{12}(r)/Hr = 1$] occurs for $\xi > 200$ [(7); see also B. Jain, *Mon. Not. R. Astron. Soc.* **287**, 687 (1997)]. In the limit $r \rightarrow 0$, our ansatz gives $-v_{12}/Hr \rightarrow [2/(3 - \gamma)]\Omega^{0.6}(1 + \alpha)$, which for the range of parameters considered is generally different from unity (although of the right order of magnitude). It is possible to improve our approximation and satisfy the small separation boundary condition by replacing $(2/3)\Omega^{0.6}$ with the expression $[(1 - \gamma/3)F\xi(r) + (2/3)\Omega^{0.6}]/[F\xi(r) + 1]$, where $F \approx 1/100$ is a fudge factor ensuring that $-v_{12}/Hr \rightarrow 1$ when $\xi \gg 100$, while the perturbative, large-scale solution remains unaffected. However, the stable clustering occurs at separations smaller than $200h^{-1}$ kpc, which is a tenth of the smallest separation we consider here. As a result, in our range of separations r , Eq. 1 is as close to fully nonlinear N -body simulations as the improvement, suggested above [see (4) and Fig. 2].

14. J. A. Willick, S. Courteau, S. M. Faber, D. Burstein, A. Dekel, *Astrophys. J.* **446**, 12 (1995).

15. J. A. Willick, et al., *Astrophys. J.* **457**, 460 (1996).

16. J. A. Willick et al., *Astrophys. J. Suppl. Ser.* **109**, 333 (1997).

17. D. Lynden-Bell et al., *Astrophys. J.* **329**, 19 (1988).

18. K. M. Górski, M. Davis, M. A. Strauss, S. D. M. White, A. Yahil, *Astrophys. J.* **344**, 1 (1989).

19. E. J. Groth, R. Juszkiewicz, J. P. Ostriker, *Astrophys. J.* **346**, 558 (1989).

20. Under realistic circumstances, one expects that gravitational growth of clustering pulls the mass with the galaxies. As a result, any clustering bias, introduced at the epoch of galaxy formation, is likely to evolve toward unity at late times, at variance with the linear bias model, where b is time independent [J. N. Fry, *Astrophys. J.* **461**, L65 (1996); P. J. E. Peebles, available at <http://xxx.lanl.gov/abs/astro-ph/9910234>]. A similar behavior was seen in N -body simulations (17). The linear bias relation $\delta^{gal} = b\delta$ is a conjecture that generally does not follow from the relation between the correlation functions $\xi^{gal} = b^2\xi$ unless we restrict our model to a narrow subclass of random fields.

21. Imagine that one of the CDM-like models is a valid description of our universe. Let us choose the dark energy and CDM (Λ CDM) model, recently simulated by the Virgo Consortium (7). It is defined by parameters $h = 0.7$, $\Omega = 0.3$, $\sigma_8 = 0.9$, and $\Omega_\Lambda = 0.7$, which is the cosmological constant's contribution to the density parameter. This model requires scale-dependent biasing because the predicted shape of $\xi(r)$ differs widely from the observed galaxy correlation function: At separations $hr \text{ Mpc}^{-1} = 10, 4, 2$, and 0.1 , the logarithmic slope of the mass correlation function reaches the values, given by $\gamma = 1.7, 1.5, 2.5$, and 1 , respectively. As we expected, however, these wild oscillations do not affect the resulting $v_{12}(r_*)$. Indeed, the N -body simulations (7) give $v_{12}(r_*) = -220 \text{ km s}^{-1}$, and substituting $\sigma_8 = 0.9$ and $\Omega = 0.3$ in Eq. 5 gives $v_{12}(r_*) = -225 \text{ km s}^{-1}$.

22. E. J. Shaya, P. J. E. Peebles, R. B. Tully, *Astrophys. J.* **454**, 15 (1995).

23. M. Davis, A. Nusser, J. A. Willick, *Astrophys. J.* **473**, 22 (1996).

24. J. A. Willick, M. A. Strauss, A. Dekel, T. Kolatt, *Astrophys. J.* **486**, 629 (1997).

25. L. N. da Costa et al., *Mon. Not. R. Astron. Soc.* **299**, 425 (1998).

26. J. A. Willick and M. A. Strauss, *Astrophys. J.* **507**, 64 (1998).

27. Y. Sigad, A. Eldar, A. Dekel, M. A. Strauss, A. Yahil, *Astrophys. J. Suppl. Ser.* **109**, 516 (1997).

28. A. G. Doroshkevich, Ya. B. Zeldovich, R. A. Sunyaev, *Sov. Astron.* **22**, 523 (1978).

29. We are grateful to L. da Costa for encouragement at the early stages of this project. We also benefited from discussions with S. Courteau, R. Durrer, K. Gór-

ski, and J. Peebles. R.J. was supported by the State Committee for Scientific Research (KBN) (Poland), the Tomalla Foundation (Switzerland), and the Poland-U.S. M. Skłodowska-Curie Fund. M.D. and A.H.J. were supported by grants from NSF and NASA. H.A.F. and R.J. were supported by NSF-EPSCOR and the General Research Fund. We thank the organizers of the summer 1997 workshop at the Aspen Center for Physics, where this work began.

12 August 1999; accepted 10 November 1999

The Changing Morphology and Increasing Deceleration of Supernova 1993J in M81

N. Bartel,^{1*} M. F. Bietenholz,¹ M. P. Rupen,² A. J. Beasley,² D. A. Graham,³ V. I. Altunin,⁴ T. Venturi,⁵ G. Umana,⁶ W. H. Cannon,^{1,7} J. E. Conway⁸

Twenty consecutive Very Long Baseline Interferometry images of supernova 1993J from the time of explosion to the present show the dynamic evolution of the expanding radio shell of an exploded star. High-precision astrometry reveals that the supernova expands isotropically from its explosion center. Systematic changes in the images may reflect a pattern of anisotropies and inhomogeneities in the material left over from the progenitor star. As the shock front sweeps up the material in the surrounding medium, it is increasingly decelerated and influenced by the material. After 5 years, the supernova has slowed to half of its original expansion velocity and may have entered the early stages of the adiabatic phase common in much older supernova remnants in the Milky Way Galaxy.

Supernova 1993J (SN1993J) (I) in the nearby galaxy M81 was the brightest optical supernova in the Northern Hemisphere since SN1954A and, at a distance of only 3.63 ± 0.36 Mpc (2), among the closest in modern history. Its progenitor star is believed to have been either an ~ 15 -solar-mass (M_\odot) supergiant that has lost a substantial portion of its hydrogen envelope to a companion in a binary system ($3, 4$) or a single $\sim 30M_\odot$ supergiant (5). Shock breakout from the explosion occurred on 28.0 March 1993 UT (6). Radio emission was detected a few days thereafter (7). An optical image of M81 superimposed on a 5-GHz Very Large Array (VLA) radio map shows the supernova in a southern spiral arm (Fig. 1). Very Long Baseline Interferometry (VLBI) observations of the young radio

source during the first 100 days showed that its size was growing with time t , with the angular radius $\theta \propto t^m$ and $m = 0.96 \pm 0.07$ (8). As the supernova expanded, its shell-like structure was revealed ($9, 10$). The expansion was found to be decelerated over a time of ~ 3 years, with estimates of m of 0.86 ± 0.02 (11) and 0.837 ± 0.025 (12). The nature of the expansion was reported (11) to be self-similar, as described in the standard model (13) of the interaction of the shock front with the circumstellar medium (CSM) left over from the mass loss of the progenitor star. The structure of the supernova would remain unchanged in this model except for a time-independent scaling factor, and the deceleration would be constant. Here, we present results from VLBI observations over 5 years (14) and show that the structure of SN1993J is changing while the expansion remains isotropic but increasingly decelerates, together reflecting departures from a self-similar evolution and revealing insights into how several-hundred-year-old supernova remnants in the Milky Way Galaxy may have evolved.

Twenty consecutive images of SN1993J were acquired from about 50 days to 5 years after the shock breakout (Fig. 2). They were made from VLBI data at 8.4 GHz phase-referenced to the core (15) of M81. The earliest image of SN1993J shows an almost

¹Department of Physics and Astronomy, York University, Toronto M3J 1P3, Ontario, Canada. ²National Radio Astronomy Observatory, Socorro, NM 87801, USA. ³Max-Planck-Institut für Radioastronomie, D-53121 Bonn, Germany. ⁴Jet Propulsion Laboratory, California Institute of Technology, Pasadena, CA 91109, USA. ⁵Instituto di Radioastronomia, CNR, 40129 Bologna, Italy. ⁶Instituto di Radioastronomia, CNR, 96017 Noto, Italy. ⁷Space Geodynamics Laboratory/CRESTech, Toronto M3J 3K1, Ontario, Canada. ⁸Onsala Space Observatory, Chalmers University of Technology, S-43992 Onsala, Sweden.

*To whom correspondence should be addressed. E-mail: bartel@yorku.ca

REPORTS

unresolved source when the supernova had a radius of just 140 micro-arc seconds (μas) or 520 astronomical units (AU) corresponding to 13 solar system radii. The first hint of the shell brightness distribution is revealed in the third image at $t = 175$ days. As the supernova expands, the shell morphology becomes more apparent. The brightness is modulated along the ridge of the shell. At first, the maximum brightness appears at eastern to southeastern azimuths, and the minimum appears on the opposite site. With time, the modulation pattern rotates counterclockwise with the peak at $t = 451$ days occurring in the south and the minimum occurring in the north. At t between 500 and 700 days, the brightness is more uniform along the ridge, except around the minimum. The minimum has now rotated to the north-northeast and appears as an opening in the shell. In addition, slight indications of an eastern and western hot spot can be discerned at $t = 686$ days. As the size increases, our relative resolution also increases, and a more complex morphology is observed. From $t = 996$ days onward, the two hot spots become more prominent and evolve in time. In addition, a southern hot spot develops and remains visible throughout the remaining images. The central region in the full-resolution map has a relatively low brightness, for, say, $t = 1693$ days, of ≤ 0.15 mJy/beam (mJy, millijansky; beam, 0.4 mas^2 ; mas, milli-arc second). This limit equals six times the root mean square (rms) of the brightness outside the supernova image and two to three times the standard error inside the shell when image fidelity considerations are taken into account. The limit corresponds to a spectral luminosity at 8.4 GHz of no more than that of the Crab pulsar nebula from the supernova explosion in 1054 A.D. However, the luminosity of a young pulsar nebula is expected to be 10 to 1000 times larger than that of the Crab nebula (16), suggesting that the center, expected to be opaque, cannot yet have become transparent by filamentation (16), provided a pulsar was formed in the first place (17). The last image at $t = 1893$ days shows a round shell with a fairly complex brightness distribution that has expanded more than 20 times over the 5 years of observations to a radius of 3.25 mas or 12,000 AU.

For a more quantitative analysis, we fit by weighted least squares a model of the two-dimensional projection of a three-dimensional shell with uniform volume emissivity to the calibrated visibility data in the u - v plane and estimated the shell's center coordinates with respect to the stationary core of M81 (15), as well as its inner and outer radii, θ_i and θ_o , respectively. Although the brightness distribution along the rim is rotationally asymmetric, the geometric shape of the shell at low brightness contours is circularly symmetric. For instance, for epochs at $t = 686$, 1532, and 1693 days, the radius of the brightness distribution at the 20% contour level,

averaged over 30° in azimuth, varies around the center coordinates of the fit shell with a rms of $<3\%$. These measurements constrain the degree of, for instance, bipolar expansion. Moderate one-sided expansion, however, would leave the shell mostly circular but move the shell center. Such expansion is therefore constrained by the degree of stationarity of the center coordinates.

A least squares linear fit for each coordinate α and δ separately gives a proper motion estimate with respect to the core of M81 of $\mu_\alpha = -9 \pm 6 \mu\text{as year}^{-1}$ and $\mu_\delta = -10 \pm 7 \mu\text{as year}^{-1}$ (18). For the above distance of 3.63 Mpc, the proper motion estimate corresponds to respective velocity components of $-100 \pm 100 \text{ km s}^{-1}$ and $-170 \pm 100 \text{ km s}^{-1}$ (no error assumed in the distance to M81). We do not consider the velocity components to be substantially different from zero. Galactic proper motion of the supernova around the core of M81 is computed from HI rotation curves (19) to be $\sim 230 \pm 160 \text{ km s}^{-1}$ and directed toward the northwest (Fig. 1). Subtracting the two velocity vectors gives a peculiar velocity of the geometric center of SN1993J of $360 \pm 140 \text{ km s}^{-1}$ toward the south and, combined with the 3% bound on circular symmetry deviations, a 1σ upper bound on any deviation from isotropic expansion of 6%.

Although the shell structure of the super-

nova can be seen in the images as early as at $t = 175$ days, only in the last several epochs was the supernova sufficiently extended on the sky for the shell thickness to be determined with useful accuracy. As an indicator of such thickness we plot the ratio θ_o/θ_i in the inset of Fig. 3. The weighted mean is $\langle \theta_o/\theta_i \rangle = 1.26 \pm 0.02$, smaller than the value of 1.4 (no errors given) estimated by others (10) but consistent with the prediction in the standard model. A weighted linear fit gives an increase of the ratio of $0.017 \pm 0.022 \text{ years}^{-1}$, which is not significant.

We determined θ_o again, with θ_o/θ_i kept fixed at 1.25 in the fits for all observations (Table 1 and Fig. 3). A weighted least squares power-law fit to the values for θ_o gives $m = 0.839 \pm 0.009$, consistent with earlier measurements (11, 12). However, the higher accuracy of the present measurements gives a reduced chi-square, $\chi_\nu^2 = 2.7$, indicating significant misfits with a probability of chance coincidence of $\leq 0.3 \times 10^{-5}$. We find that a self-similar expansion characterized by a constant deceleration parameter m is not realized for SN1993J. At early times up to, say, $t = 306$ days, the supernova expands with $m = 0.937 \pm 0.020$ ($\chi_\nu^2 = 0.85$), confirming our earlier value (8) with a more than threefold increase in accuracy and indicating a slight deceleration of the shock front in the

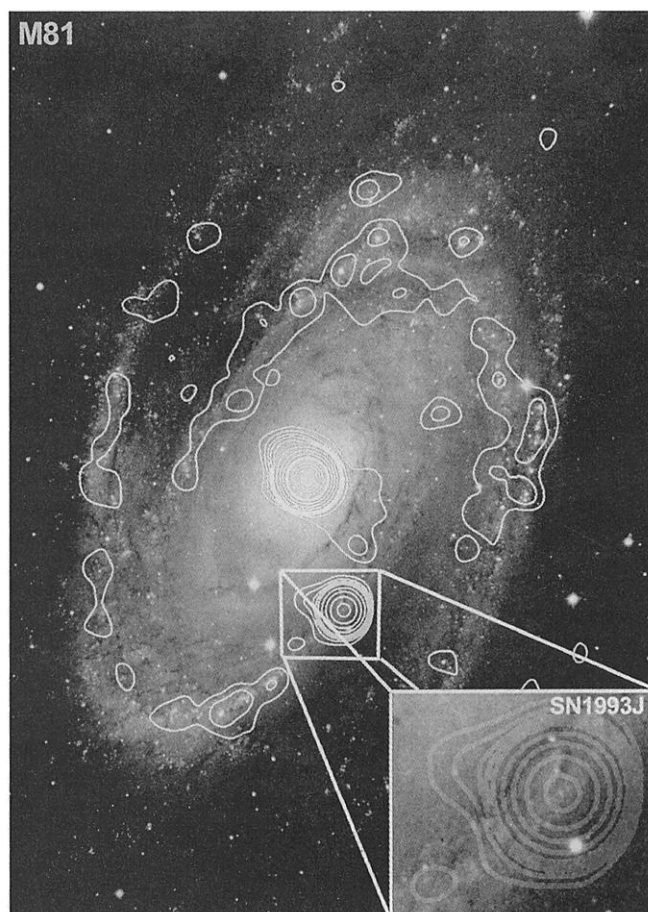


Fig. 1. The galaxy M81 at 5.0 GHz observed with the VLA in the D array on 15 November 1997, superimposed on an optical image (31). The radio contour levels are at 0.14, 0.3, 0.5, 0.7, 1, 2, 4, 8, 15, 20, 40, and 80 mJy/beam. The brightest source is the nucleus of M81 at 120 mJy/beam. SN1993J is the second brightest source located approximately south of the center. The inset shows an enlarged portion of the radio and optical images at the location of SN1993J with the progenitor of SN1993J visible at the radio brightness peak. The width of the box corresponds to 2 arc min at the sky. North is up, and east is to the left.

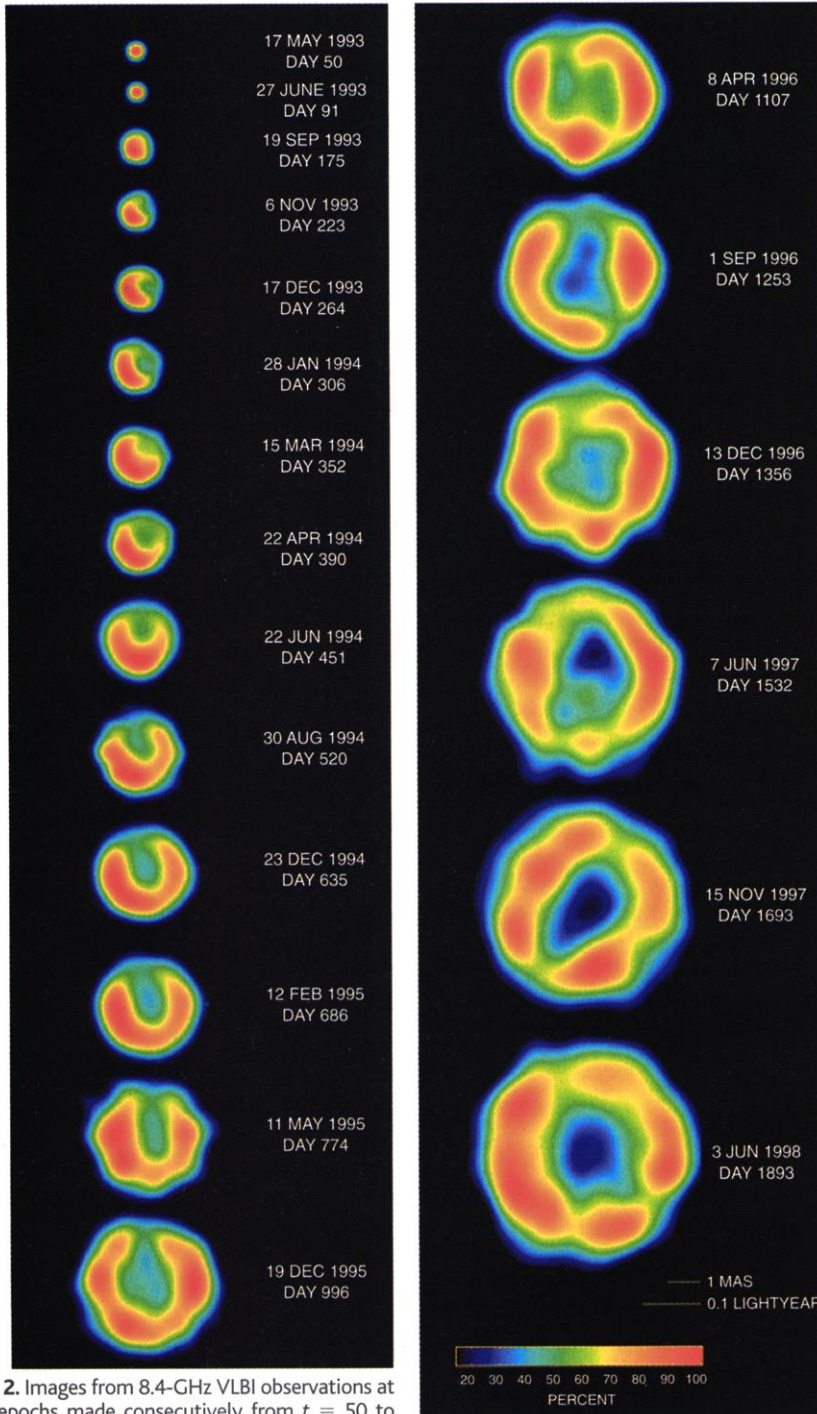


Fig. 2. Images from 8.4-GHz VLBI observations at 20 epochs made consecutively from $t = 50$ to 1893 days after shock wave breakout (32). The total flux density reaches a peak of ~ 100 mJy at $t = 100$ days and decreases thereafter to ~ 18 mJy for the last map. The convolving beam is conservatively chosen to be circular for each map with the full width at half maximum (FWHM) approximately equal to or larger than the FWHM of the "dirty beam" along its major axis. It starts with a FWHM of 0.5 mas, increases steadily to 0.9 mas for the midterm map at $t = 996$ days, and then increases again to 1.15 mas for the last map. This procedure minimizes deconvolution distortions and brightness structure misinterpretations and provides for a smooth appearance of the structural evolution of the supernova. The color brightness scale is normalized separately to the peak of each image. The peak brightnesses for the representative first, middle, and last map are 15, 1.9, and 0.8 mJy/beam, respectively, and the corresponding rms values of the background noise are 0.10, 0.09, and 0.03 mJy/beam. Differences in features are significant if they are larger than $\sim 10\%$ for the first-year maps and $\sim 20\%$ from then onward.

first months after the shock breakout. With the distance of 3.63 Mpc, the early velocity is equal to the largest expansion velocity v_{\max}

seen in the optical spectra. For, say, $t = 19$ days, our fit gives $17,600 \pm 500$ km s^{-1} , compared with $v_{\max} = 18,000 \pm 1000$ km

Table 1. SN1993J size determinations.

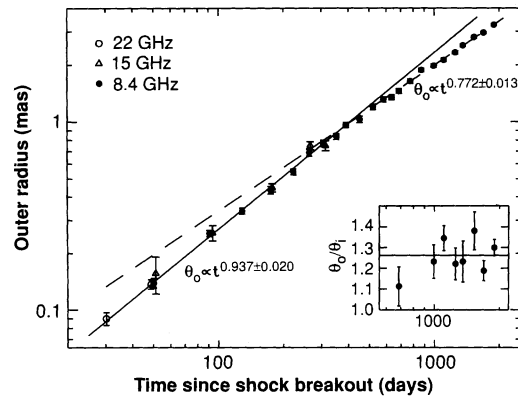
Date	Age* (days)	Frequency (GHz)	Angular radius† (μas)
27 Apr 1993	30	22	90 ± 7
17 May 1993	50	22	137 ± 8
17 May 1993	50	15	157 ± 35
17 May 1993	50	8.4	139 ± 8
27 Jun 1993	91	15	257 ± 24
27 Jun 1993	91	8.4	256 ± 10
4 Aug 1993	129	8.4	337 ± 12
19 Sep 1993	175	15	447 ± 23
19 Sep 1993	175	8.4	435 ± 20
6 Nov 1993	223	8.4	544 ± 20
17 Dec 1993	264	15	749 ± 37
17 Dec 1993	264	8.4	689 ± 30
28 Jan 1994	306	15	749 ± 37
28 Jan 1994	306	8.4	769 ± 30
15 Mar 1994	352	8.4	836 ± 30
22 Apr 1994	390	8.4	961 ± 30
22 Jun 1994	451	8.4	1030 ± 30
30 Aug 1994	520	8.4	1197 ± 40
31 Oct 1994	582	8.4	1311 ± 40
23 Dec 1994	635	8.4	1346 ± 40
12 Feb 1995	686	8.4	1453 ± 40
11 May 1995	774	8.4	1675 ± 40
18 Aug 1995	873	8.4	1877 ± 40
19 Dec 1995	996	8.4	1979 ± 40
8 Apr 1996	1107	8.4	2125 ± 40
1 Sep 1996	1253	8.4	2328 ± 40
13 Dec 1996	1356	8.4	2537 ± 40
7 Jun 1997	1532	8.4	2810 ± 40
15 Nov 1997	1693	8.4	2957 ± 40
3 Jun 1998	1893	8.4	3254 ± 40

*Time since shock breakout on 28.0 March 1993 UT. †The angular outer radius θ_o of a three-dimensional shell model, see text (18).

s^{-1} from the blue edge of the H_{α} hydrogen absorption trough (20). Vice versa, we get a direct distance determination to M81 of $v_{\max}/\dot{\theta}_o = 3.7 \pm 0.4$ Mpc (21). The deceleration grows later on. For the time period from $t = 582$ days to our last epoch at $t = 1893$ days, $m = 0.772 \pm 0.013$ ($\chi^2_{\nu} = 1.2$), which is different from m at early times by 7σ (22) and indicates a change of the physical parameters in the shock front region (Fig. 3). A changing deceleration rate has not been directly monitored for any other supernova, although for SN1987A, it could be inferred that a change had occurred before the first size measurements (23).

From these results, a coherent picture of the evolution of SN1993J can be derived. From early on, the supernova expanded isotropically (at least in projection) within 6% and with the shock front appearing circular, even within 3%. The evolving brightness distribution, however, is azimuthally asymmetric and more complex than expected for a self-similar expansion. Changes in the brightness distribution could be caused by irregularities in the ejecta, such as fluctuations of the density distribution coupled with distortions in the velocity field of the hydrogen gas. However, given the high degree of circularity of the images, such irregularities may not be the dominant cause of the structural changes.

Fig. 3. The angular outer radius θ_o of the shell model from Table 1, plotted against time. The dashed and solid diagonal lines represent weighted least-squares fits ($\theta_o \propto t^m$) to the 14 data points of the early eight epochs ($t \leq 306$ days) and to the 12 data points of the latest 12 epochs ($t \geq 582$ days). For the latest epochs, the standard errors of θ_o are only half as large as the symbols. (**Inset**) The ratio of θ_o to the inner radius θ_i for several of the last observations for which both θ_o and θ_i could be estimated with useful accuracy. The horizontal line represents the weighted mean of θ_o/θ_i from these epochs. Error bars indicate SE (18).



Another possible cause for the structural changes may be changes in the magnetic field. Probably more important are deviations from isotropy and homogeneity of the CSM in the form of local condensations in the wind from the progenitor star possibly caused by its binary nature. The shock front overruns this stellar wind with a speed up to ~ 2000 times larger. It can thus act as a “time machine,” by recording, in just a few years and in reverse, the wind history over the period of $\sim 10,000$ years before the star died.

The expansion was already slightly decelerated at the time of the first observations, and its deceleration increases subsequently, indicating a change in the interaction between the shock front and the CSM. In particular, with the assumption that the standard model gives an approximate description of the interaction region at least for individual time segments, the deceleration is related to the density profiles of the supernova ejecta, $\rho_{\text{SN}} \propto r^{-n}$, and of the surrounding CSM, $\rho_{\text{CS}} \propto r^{-s}$, with r as the radius from the supernova center and $m = (n - 3)/(n - s)$ (24). The expanding shock front sweeps away the obscuring layers, giving a time dependence for the opacity due to external free-free absorption of $\tau \propto t^\delta$, with $\delta = -(2s - 1)m$ and $n = (6 + \delta - m)/[2(1 - m)]$. With $\delta = -1.99^{+0.38}_{-0.16}$ determined from the radio light curves (25), our early expansion value for m gives $s = 1.56^{+0.10}_{-0.20}$ and $n = 24^{+12}_{-6}$, consistent with the interpretation of early x-ray emission (26). For the later time interval, 2 to 5 years after the explosion, the parameter δ is not well determined. If we assume that it has not changed, then $s = 1.79^{+0.11}_{-0.25}$ and $n = 7.1^{+0.5}_{-0.9}$. A more elaborate model, with synchrotron self-absorption included, gives $s = 2$ being consistent with the data for all times (27). With this value, n changes from early to late times from 18^{+7}_{-4} to 6.4 ± 0.3 .

These results represent a shock front with an initially steep density profile that relaxes its steepness after 1 year as the shock front sweeps through, and is progressively decelerated by, the CSM. The latter has a density profile close to $s = 2$, expected for an isotropic CSM gen-

erated by a time-constant ratio of mass loss to wind velocity, \dot{M}_w/w , of the progenitor. Or, for the alternative scenario with $s = 1.56$, the profile is somewhat flatter (at least during the first year), indicating a decreasing ratio (25), $\dot{M}_w/w \propto t^{-0.44}$, at least for the last 1500 years before the star died. Our images show asymmetries in the brightness distribution resembling a horseshoe pattern that rotates with time during the first ~ 600 days and systematically changes in a more complex way afterward, indicative of a pattern of deviations from isotropy and time constancy. Perhaps \dot{M}_w/w was systematically changing angularly and temporally but on average remaining constant for $s = 2$ or decreasing with time for $s = 1.56$. Or, perhaps more plausibly, the density profile of the CSM may have been modified by the fast wind of an early-type companion (28), giving rise to the asymmetric and rotating brightness pattern seen in the early images. The change in the deceleration of the expansion after ~ 1 year may indicate the location at which such modification was no longer dominant. However, a direct sign of the purported binary nature of the progenitor, for instance, in the form of a suggested disklike structure (29) of the CSM, is hard to discern in the images. Two-dimensional hydrodynamic simulations may be needed to interpret the details of the images accurately.

After 5 years, the velocity of the shock front has slowed down to $\sim 8500 \text{ km s}^{-1}$, less than half of its value during the first 3 weeks. Therefore, the mass of the CSM swept up by the shock front, M_{sw} , is expected to be comparable to or larger than the mass in the hydrogen shell, M_{shell} . With $\dot{M}_w = 5 \times 10^{-5} M_\odot \text{ years}^{-1}$ for $w = 10 \text{ km s}^{-1}$ from radio light curve fits (27) and $s = 2$, we get $M_{\text{sw}} \sim 0.3 M_\odot$. This value increases by 30% for the alternative scenario with $s = 1.56$ during the first year instead and the above value for \dot{M}_w occurring for a time of 120 years before the explosion (25). In any case, this value is too small in comparison to $M_{\text{shell}} \sim 3 M_\odot$, suggested for the single-star model (5). An unrealistically high value of \dot{M}_w/w would have to be assumed for $M_{\text{sw}} \geq M_{\text{shell}}$. The value of M_{shell} is, however, comparable

to the relatively small estimates of $0.2 M_\odot$ to $0.4 M_\odot$ (4, 30) that remained after mass transfer to the companion for binary models. Therefore, and because of the growing deceleration, SN1993J has finished the free-expansion stage and appears to have entered the early stages of adiabatic expansion, where its evolution is dominated by the swept-up material of the CSM, and the deceleration parameter approaches $m = 0.4$. Several much older galactic supernova remnants are believed to be in this stage, interacting instead with the interstellar medium. However, their evolution could be monitored only over $<10\%$ of their lifetime. SN1993J has been monitored over nearly 100% of its life and, after only 5 years, indicates how much older supernova remnants in our own galaxy may have evolved.

References and Notes

1. J. Ripero and F. Garcia, *IAU Circ.* **5731**, 1 (1993).
2. Distance from cepheid observations; see W. L. Freedman et al., *Astrophys. J.* **427**, 628 (1994).
3. Ph. Podsiadlowski, J. J. L. Hsu, P. C. Joss, R. R. Ross, *Nature* **364**, 509 (1993); K. Nomoto et al., *IAU Symp.* **165**, 119 (1996).
4. S. E. Woosley, R. G. Eastman, T. A. Weaver, P. A. Pinto, *Astrophys. J.* **429**, 300 (1994).
5. P. Höflich, N. Langer, M. Duschinger, *Astron. Astrophys.* **275**, L29 (1993).
6. J. C. Wheeler et al., *Astrophys. J.* **417**, L71 (1993).
7. G. G. Pooley and D. A. Green, *Mon. Not. R. Astron. Soc.* **264**, L17 (1993); K. W. Weiler, R. A. Sramek, S. D. Van Dyk, N. Panagia, *IAU Circ.* **5752**, 1 (1993); J. A. Phillips and S. R. Kulkarni, *IAU Circ.* **5775**, 1 (1993).
8. N. Bartel et al., *Nature* **368**, 610 (1994).
9. J. M. Marcaide et al., *Nature* **373**, 44 (1995); N. Bartel, M. F. Bietenholz, M. P. Rupen, *Proc. Natl. Acad. Sci. U.S.A.* **92**, 11374 (1995).
10. J. M. Marcaide et al., *Science* **270**, 1475 (1995).
11. J. M. Marcaide et al., *Astrophys. J.* **486**, L31 (1997).
12. M. P. Rupen et al., *IAU Colloq.* **164**, 355 (1998).
13. R. A. Chevalier, *Astrophys. J.* **258**, 790 (1982).
14. The observations were made at 8.4 GHz and, early on, also at 15 and 22 GHz, with a global VLBI array of between 11 and 18 radio telescopes located in Europe, North America, and Hawaii. The antennas with their diameters, affiliations, and locations are as follows: VLA [equivalent diameter 130 m; National Radio Astronomy Observatory (NRAO); near Socorro, NM], Effelsberg (100 m; Max-Planck-Institut für Radioastronomie; Effelsberg, Germany), Deep Space Station (DSS) 63 [70 m; NASA/Jet Propulsion Laboratory (JPL); Robledo, Spain], DSS 14 (70 m; NASA/JPL; Goldstone, CA), ARO (46 m; ISTS/York University and Geomatics/NRC; Algonquin Park, Ontario, Canada), Greenbank (43 m; NRAO; Greenbank, WV), Medicina [32 m; Instituto di Radioastronomia—Consiglio Nazionale delle Ricerche (IdR-CNR); Medicina, Italy], Noto (32 m; IdR-CNR; Noto, Italy), and VLBA (25 m, NRAO, 10 antennas spread out across the United States). The data were recorded with the VLBA and either the MKIII (mode A) or the MKIV VLBI systems at rates of 128 or 256 Mbits s^{-1} . At each station, a hydrogen maser was used to set the frequency standard for the local oscillator chain and to “time tag” the recorded data. The data were taken by switching the VLBI array from SN1993J to the radio nucleus of M81 in a repeated cycle of ~ 3 -min duration. This mode was chosen for using phase-referenced mapping for superior sensitivity, data calibration, and imaging, and for accurate astrometric measurements. The data were correlated with the NRAO VLBA processor at Socorro, NM. The analysis was carried out with NRAO’s Astronomical Image Processing System (AIPS) and a modified version of the AIPS routine OMFIT.

15. M. F. Bietenholz *et al.*, *Astrophys. J.* **457**, 604 (1996); M. F. Bietenholz, N. Bartel, M. P. Rupen, *Astrophys. J.*, in press.
16. R. Bandiera, F. Pacini, M. Salvati, *Astrophys. J.* **285**, 134 (1984).
17. W. Kundt, *Fundam. Cosmic Phys.* **20**, 1 (1998).
18. All uncertainties in this paper are standard errors. The standard errors of fit parameters were calculated to reflect a χ^2_ν of unity in case the measured $\chi^2_\nu > 1$. The standard errors of individual data points had statistical and estimated systematic contributions added in quadrature.
19. A. H. Rots and W. W. Shane, *Astron. Astrophys.* **45**, 25 (1975).
20. S. R. Trammell, D. C. Hines, J. C. Wheeler, *Astrophys. J.* **414**, L21 (1993); J. M. Lewis *et al.*, *Mon. Not. R. Astron. Soc.* **266**, L29 (1994). At later times, the maximum velocity could not be determined reliably from the H α absorption trough because of blending effects with newly developed emission lines.
21. The standard error includes the errors from the optical velocity and the rate of change of the VLBI angular radius, and the upper limit of deviations from isotropic expansion (N. Bartel *et al.*, in preparation).
22. We investigated the model dependence of our result and found that the asymmetric brightness distributions, possible shell thickness variations, and opacity effects would not alter the significance of the change of the deceleration rate by more than $\sim 1\sigma$. Our results are in conflict with a measurement of $m = 0.89 \pm 0.03$ for the late time from $t = 541$ to 1304 days (17). The significant discrepancy could be due to these authors not having used the more sensitive and convolution-free method of model fitting. Their method of convolving the source with a beam increasing in size $\propto t$ (implicitly assuming $m = 1$) and measuring the radius for a particular contour level (50%) biases the determination of m toward values of unity (as they note) and decreases the sensitivity of detecting deviations from a self-similar expansion.
23. B. M. Gaensler *et al.*, *Astrophys. J.* **479**, 845 (1997).
24. R. A. Chevalier, *Astrophys. J.* **259**, 302 (1982).
25. S. D. Van Dyk, K. W. Weiler, R. A. Sramek, M. P. Rupen, *Astrophys. J.* **432**, L115 (1995).
26. T. Suzuki and K. Nomoto, *Astrophys. J.* **455**, 658 (1995); C. Fransson, P. Lundqvist, R. A. Chevalier, *Astrophys. J.* **461**, 993 (1996).
27. C. Fransson and C.-I. Björnsson, *Astrophys. J.* **509**, 861 (1998).
28. H. Nussbaumer and R. Walder, *Astron. Astrophys.* **278**, 209 (1993).
29. P. Lundqvist, in *Circumstellar Media in the Late Stages of Stellar Evolution*, R. E. S. Clegg, I. R. Stevens, W. P. S. Meikle, Eds. (Cambridge Univ. Press, Cambridge, 1994), pp. 213–220.
30. J. C. Houck and C. Fransson, *Astrophys. J.* **456**, 811 (1996).
31. A. Sandage, *The Hubble Atlas of Galaxies* (Carnegie Institution of Washington, Washington, DC, 1961).
32. The sequence of radio images has been made into a movie of exploding star SN1993J (available at <http://aries.phys.yorku.ca/~bartel/SNmovie.html>).
33. Research at York University was partly supported by the Natural Sciences and Engineering Research Council of Canada. NRAO is a facility of NSF operated under cooperative agreement by Associated Universities, Inc. The NASA/JPL Deep Space Network is operated by JPL/California Institute of Technology, under contract with NASA.

16 June 1999; accepted 23 November 1999

Protein Interaction Mapping in *C. elegans* Using Proteins Involved in Vulval Development

Albertha J. M. Walhout,^{1*} Raffaella Sordella,¹ Xiaowei Lu,^{2†}
James L. Hartley,³ Gary F. Temple,³ Michael A. Brasch,³
Nicolas Thierry-Mieg,^{1,4} Marc Vidal^{1*†}

Protein interaction mapping using large-scale two-hybrid analysis has been proposed as a way to functionally annotate large numbers of uncharacterized proteins predicted by complete genome sequences. This approach was examined in *Caenorhabditis elegans*, starting with 27 proteins involved in vulval development. The resulting map reveals both known and new potential interactions and provides a functional annotation for approximately 100 uncharacterized gene products. A protein interaction mapping project is now feasible for *C. elegans* on a genome-wide scale and should contribute to the understanding of molecular mechanisms in this organism and in human diseases.

Complete genome sequences are available for *Escherichia coli*, *Saccharomyces cerevisiae*, and *C. elegans*, and are expected soon for other model organisms and humans (1). In addition to facilitating the identification and cloning of genes and providing valuable insights on evolution, this information is likely to change the way biological questions are addressed. It is becoming possible to study molecular mechanisms globally in the context of complete sets

of genes, rather than analyzing genes individually. For example, DNA microarrays and chips can be used to monitor simultaneously the expression of nearly all genes of an organism (2). However, the function of most gene products predicted from sequencing projects is still completely uncharacterized, and it is widely accepted that this limitation needs to be overcome before full advantage can be taken of complete genome sequences. Functional assays aimed at characterizing the cellular localization of proteins, their spatial and temporal expression patterns, and their potential interacting partners should provide a backbone of functional annotations from which new biological questions can be formulated (3). Because the number of unannotated gene products in each model organism ranges from thousands to tens of thousands, it is important to develop standardized functional assays in which the same procedure can be applied to many proteins at a time, allowing utilization of high-throughput procedures.

Protein-protein interactions are crucial for many biological processes. Therefore, the knowledge of potential interactions involving otherwise uncharacterized proteins may provide insight into their function. The two-hybrid system, a standardized functional assay, facilitates the identification of potential protein-protein interactions and has been proposed as a method for the generation of protein interaction maps (4–7). Before the approach can be applied on a genome-wide scale, however, conceptual and technical issues need to be addressed. Conceptually, the biological information generated by two-hybrid analyses is often questioned because of the inherent artificial nature of the assay. Therefore, this method should be tested in a model organism using groups of proteins for which functional data are available. Technically, the cloning of open reading frames (ORFs) into appropriate expression vectors with the current techniques is laborious and expensive when dealing with hundreds or thousands of genes. Consequently, methods to standardize this process are required. Furthermore, it is necessary to decide upon a format in which the interaction data will be made available to the research community. Finally, it will be necessary to develop methods to determine the biological relevance of the potential interactions identified.

To address the issue of the potential biological relevance of protein interaction maps, we selected *C. elegans* as a model organism (8). The nearly complete *C. elegans* genome sequence led to the prediction of $\sim 20,000$ gene products of which approximately 700 have been functionally characterized [for example, (9)]. As a starting point, we chose to focus on *C. elegans* genes involved in the regulation of vulval development. At least four different pathways function coordinately to form a single vulva in the adult hermaphrodite, including a receptor tyrosine kinase (RTK)/Ras pathway (RTK/Ras), a Notch pathway (Notch), and two

¹Massachusetts General Hospital Cancer Center, Charlestown, MA 02129, USA. ²Howard Hughes Medical Institute, Massachusetts Institute of Technology, Cambridge, MA 02139, USA. ³Life Technologies Inc., Rockville, MD 20850, USA. ⁴Laboratoire LSR-IMAC, 38402 St-Martin-D'Herès Cedex, France.

*Present address: Dana Farber Cancer Institute, Department of Genetics, Harvard Medical School, Boston, MA 02115, U.S.A.

†Present address: Department of Anatomy, University of California San Francisco, San Francisco, CA 94143, USA.

‡To whom correspondence should be addressed. E-mail: Marc_Vidal@DFCI.Harvard.edu